



The influence of CeO₂ abrasive size on the performance of photocatalytic assisted chemical-mechanical polishing by Y/Pr co-doping strategy

Ning Xu ^{a,b,c,d,*}, Yuxin Luo ^{a,b}, Yu Lin ^{a,b}, Jiahui Ma ^{a,b}, Yongping Pu ^{a,b}

^a School of Material Science and Engineering, Shaanxi University of Science & Technology, Xi'an, Shaanxi Province 710021, China

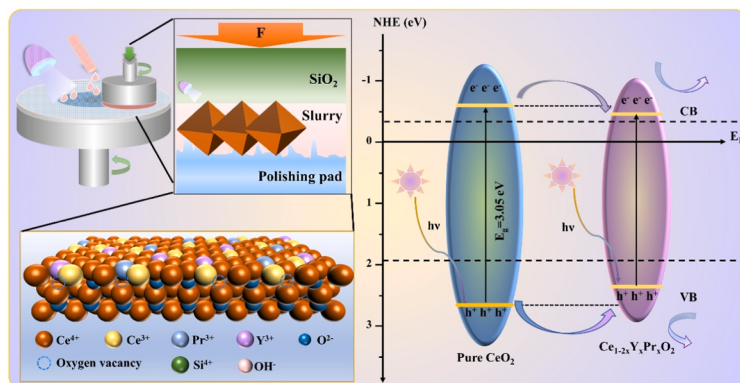
^b Shaanxi Key Laboratory of Green Preparation and Functionalization for Inorganic Materials, Xi'an, Shaanxi Province 710021, China

^c Key Laboratory of Auxiliary Chemistry and Technology for Chemical Industry, Ministry of Education, Shaanxi University of Science and Technology, Xi'an, Shaanxi Province 710021, China

^d Shaanxi Collaborative Innovation Center of Industrial Auxiliary Chemistry and Technology, Shaanxi University of Science and Technology, Xi'an, Shaanxi Province 710021, China



GRAPHICAL ABSTRACT



ARTICLE INFO

Keywords:
Photocatalytic-assisted chemical-mechanical polishing (PCMP)
Co-doping
Removal rate
CeO₂ abrasive

ABSTRACT

The synergistic effect of photochemical oxidation activity and tribochemical ability of CeO₂ material is a necessary prerequisite for the formation of photocatalytic assisted chemical-mechanical polishing (PCMP) abrasive system. However, it is precisely due to the large band gap (~ 3.2 eV) of CeO₂ and the high recombination rate of photogenerated carriers that the improvement of the photocatalytic oxidation activity of traditional CeO₂ photocatalysts is greatly limited, thus preventing the further wide application of cerium-based abrasives in PCMP. Based on this, a series of Ce_{1-2x}Y_xPr_xO₂ abrasives were synthesized by molten salt method to improve the performance of cerium oxide based polishing paste with PCMP. The physicochemical properties of Ce_{1-2x}Y_xPr_xO₂ samples were analyzed by a series of characterization methods. The results show that Ce_{1-2x}Y_xPr_xO₂ abrasive has a normal octahedral shape with a particle size of 190 ~ 260 nm. With the increase of doping amount, the particle size of abrasive decreases gradually, but the photocatalytic activity increases. Compared with undoped CeO₂ abrasives, the removal rate (RR = 932.42 nm/min) of quartz glass by Ce_{1-2x}Y_xPr_xO₂ abrasive was increased by about 87.10%. At the same time, the surface quality has been

* Corresponding author at: School of Material Science and Engineering, Shaanxi University of Science & Technology, Xi'an, Shaanxi Province 710021, China.
E-mail address: xuning@sust.edu.cn (N. Xu).

significantly improved. A smooth, flawless and low roughness surface was obtained. The improvement in surface quality can be demonstrated by reducing surface roughness (R_a). The R_a of quartz glass decreased to 0.36 nm after $\text{Y}^{3+}/\text{Pr}^{3+}$ co-doped CeO_2 abrasive by PCMP (the original R_a of glass was 1.08 nm). It was considered that the size of the abrasive had a close relationship with the surface quality and the RR of the polished glass. Meanwhile, characteristic co-doping strategy was conducive to increase the Ce^{3+} and oxygen vacancy concentration of CeO_2 particles, which optimized the separation efficiency of the photogenic carrier of the photocatalyst. This further promoted the generation of oxidizing active substances in the polishing slurry, and therefore expediting the formation and removal of the chemical reaction soft layer. The removal mechanism of $\text{Ce}_{1-2x}\text{Y}_x\text{Pr}_x\text{O}_2$ abrasives in PCMP process was discussed.

1. Introduction

Chemical-mechanical polishing (CMP) technology is a kind of technology that realizes the global planarization of ultra-precision surface by the synergistic action of chemical reaction and mechanical wear [1]. It has a very wide application in the field of integrated circuit and optical device manufacturing. Traditional chemical-mechanical polishing processes usually involve the use of a large number of chemicals and high energy consumption equipment, resulting in environmental problems and energy waste [2]. To overcome these challenges, new green chemical-mechanical polishes have been developed for copper [1], sapphire [3], diamond [4], alloys [5], silicon [6] and molten silica [7]. Using the developed green CMP, the atomic surface implementation is used in the semiconductor, optoelectronics and aerospace industries [8]. These studies are a great contribution to traditional CMP and manufacturing [9]. Furthermore, in order to solve these problems, researchers began to look for more environmentally friendly and energy efficient surface treatment methods. In addition, with the development of technology and the expansion of market demand, the quality requirements for material surfaces are also getting higher and higher. In some applications, such as optoelectronic device manufacturing, small surface defects and contamination can cause device performance degradation, and it is necessary to find a way to remove surface defects and contamination more effectively. Therefore, some auxiliary chemical-mechanical polishing technology came into being, such as: photocatalytic assisted chemical-mechanical polishing (PCMP) [10], ultrasonic assisted chemical-mechanical polishing [11–16], electrocatalytic-assisted chemical-mechanical polishing (ECMP) [17–21], magnetorheological finishing (MRF) [22–28], plasma-assisted chemical-mechanical polishing [29–31] and so on.

Photocatalytic oxidation is an environmentally friendly and high-efficiency technology, which has the advantages of less secondary pollution, low energy consumption, high efficiency and simple operation [32]. Photocatalytic assisted chemical-mechanical polishing uses photocatalytic reactions under light irradiation to enhance the effect of chemical-mechanical polishing, in order to achieve efficient, environmentally friendly and low-cost surface treatment. In the usual PCMP process, light irradiation of polishing slurry containing photocatalytic abrasives is crucial in workpiece surface removal [33,34]. PCMP abrasive system has photocatalytic performance in addition to mechanical wear performance, compared with traditional CMP. Therefore, the choice of abrasive system is essential to the performance of PCMP.

Currently, the lanthanide sequences are being analyzed to evaluate their effectiveness as new elements for chemical-mechanical polishing. Among them, cerium (Ce) is the most potential candidate because it has the environmentally friendly [35–38]. Ceria (CeO_2) is considered to be one of the most efficient polishing abrasives due to its uniform tribo-chemical activity and chemical tooth effect. Due to its volatile valence states (Ce^{4+} and Ce^{3+}), CeO_2 is also considered to be a rare earth semiconductor photocatalyst [29]. Notably, it is the synergistic effect of the photochemical oxidation activity and tribo-chemical ability of CeO_2 material that is the necessary pre-condition for the formation of PCMP abrasive system. Nevertheless, it is precisely the large band gap (~ 3.2 eV) of CeO_2 and the high recombination rate of photogenerated carriers,

which greatly limits the improvement of the photocatalytic oxidation activity of traditional CeO_2 photocatalysts [10]. Therefore, increasing the photocatalytic activity of CeO_2 sample is of great significance for the successful application of ceria-based abrasive in PCMP. It is currently concluded that the photocatalytic property of photocatalyst can be efficaciously regulated with modulating the photoinduced electron-hole recombination rate. Although it is well known that excellent surface quality and material removal rates depend on the chemical reactivity between the abrasive and the substrate surface in addition to the mechanical wear capacity of the abrasive. However, the precise removal mechanism of CeO_2 abrasives when polishing SiO_2 substrates is still controversial, which is an urgent problem to be solved in PCMP [39]. Hence, it is very important to research and regulate the intrinsic properties of abrasives to improve the performance of PCMP. Ma et al. [29] synthesized pure cubic CeO_{2-x} nanoparticles by pulsed plasma fluid phase method (PPL) in one step. Compared with commercial samples, the prepared samples have higher photocatalytic activity and better polishing properties for quartz glass, with the RR of 520 nm/h. This is attributed to high Ce^{3+} content and/or small particle size. Chen et al. [10] synthesized three-layer polystyrene/polyaniline/cerium dioxide (PS/PANI/ CeO_2) abrasives for PCMP. Compared with PS/ CeO_2 , the RR of the synthesized abrasives is improved by about 69%. This may be due to the optimized contact interface between the surface of the workpiece and the abrasive, in addition to the synergistic effect of the PANI- CeO_2 heterojunction, which improves the photocatalytic activity and the RR . Chen et al. [40] prepared $\text{mSiO}_2 @ \text{CeGdO}_2$ abrasives with strong light chemical and tribo-chemical activity and obtained excellent quartz surface quality ($R_a = 1.37 \pm 0.07 \text{ \AA}$) and RR ($145.6 \pm 20.2 \text{ nm/min}$) in PCMP tests compared to commercial CeO_2 . They believe that this is a combination of the increase of oxygen vacancy and ceria and the optimization of the interface contact state. These works lay the foundation for optimizing the functional abrasive system of PCMP by surface modification and structural adjustment of the abrasive.

Sabia and Stevens found that in addition to Ce^{4+} , there was a certain amount of Ce^{3+} on the surface of CeO_2 grinding particles during polishing. More studies have shown that the increase of Ce^{3+} concentration on CeO_2 abrasive surface significantly enhances its chemical action on SiO_2 substrate, thus enhancing its removal efficiency. The properties of CeO_2 materials can be easily manipulated by exogenous doping within the framework of their stable crystal structure to construct solid solutions [41]. Schmitt et al. [41] believed that cations with similar ionic radius but different valency to Ce^{4+} were compensated by the generation of point defects, and doping trivalent cations was more conducive to the formation of Ce^{3+} in CeO_2 structure. Because Y^{3+} and Pr^{3+} have ionic radii similar to Ce^{4+} , it is easier to enter the CeO_2 lattice. Inspired by previous work [29, 39, 40, 42–45], this paper reports some of our efforts in the design and manufacture of Y and Pr co-doped cerium dioxide materials as streamlined functional abrasives for PCMP processing technology. It is an effective strategy to alter the microstructure of CeO_2 -based abrasives by co-doping and design different sizes of abrasives to improve the chemical reactivity, which is strongly connected with PCMP performance. Co-doping is used to prolong the recombination rate of photogenerated carriers and effectively enhance the charge carriers separation efficiency, consequently improving the

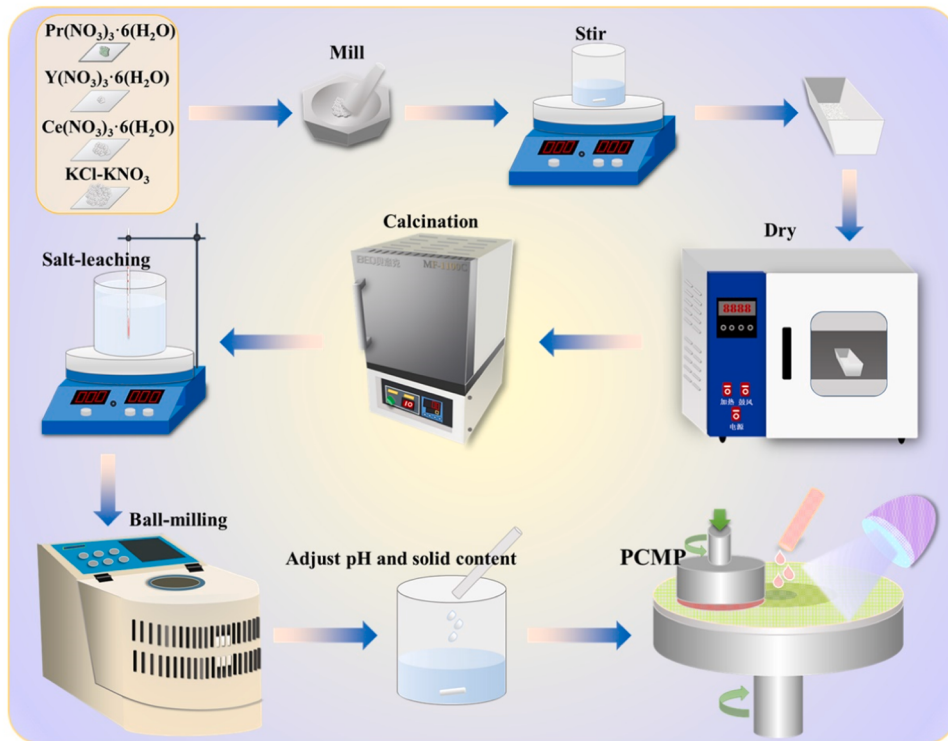


Fig. 1. Synthesis diagram of $\text{Ce}_{1-x}\text{Y}_x\text{Pr}_x\text{O}_2$ samples.

photocatalytic activity of the synthesized materials [46–48]. The purpose of this study is to heighten the performance of CeO_2 -based functional abrasives in PCMP through the co-doping strategy.

2. Material and methods

2.1. Chemicals

Cerium nitrate hexahydrate ($\text{Ce}(\text{NO}_3)_3 \cdot 6 \text{ H}_2\text{O}$) was purchased from Shanghai Maclin Biochemical Technology Co., LTD. (China). Yttrium nitrate hexahydrate ($\text{Y}(\text{NO}_3)_3 \cdot 6 \text{ H}_2\text{O}$) was analytical reagents, which was purchased from Sinophelic Medicine Holding Chemical Reagent Co., LTD. Praseodymium nitrate hexahydrate ($\text{Pr}(\text{NO}_3)_3 \cdot 6 \text{ H}_2\text{O}$) was purchased from Alfa Essa (China) Chemical Co., LTD. Potassium chloride (KCl) and potassium nitrate (KNO_3) were all analytical reagents, which were purchased from Sinophelic Medicine Holding Chemical Reagent Co., LTD. The analytical reagent ethanol was purchased from Tianjin Fuyu Fine Chemical Co., LTD. Home-made deionized water was used throughout the experiment. All the chemicals are used without further purification.

2.2. Synthesis of $\text{Ce}_{1-x}\text{Y}_x\text{Pr}_x\text{O}_2$ samples

$\text{Ce}_{1-x}\text{Y}_x\text{Pr}_x\text{O}_2$ abrasives were synthesized by molten salt method. The synthesis steps are as follows: first, the weighed $\text{Ce}(\text{NO}_3)_3 \cdot 6 \text{ H}_2\text{O}$, $\text{Y}(\text{NO}_3)_3 \cdot 6 \text{ H}_2\text{O}$, $\text{Pr}(\text{NO}_3)_3 \cdot 6 \text{ H}_2\text{O}$, KCl and KNO_3 were fully ground in an agate mortar, anhydrous ethanol was added, and then the raw materials were stirred for 30 min at a rotating speed of 400 r/min with magnetic force to fully mix. The raw material was placed in an alumina crucible and dried in remain unchanged temperature drying tunnel at 80 °C to make all the anhydrous ethanol volatilize. Then, it was roasted in MF-1100 C-S Muffle furnace (Anhui Beick Equipment Technology Co., LTD) at 850 °C for 4 h. The molten-salt ($\text{KNO}_3\text{-KCl}$) in the hybrid was eliminated with deionized water for 4–5 times to obtain $\text{Ce}_{1-x}\text{Y}_x\text{Pr}_x\text{O}_2$ abrasives at room temperature, as shown in Fig. 1.

2.3. Photocatalytic activity test

A 300 W xenon lamp (PLS-SXE300, Beijing Perfect Light) was used to study the photocatalytic performance of Tetracycline (TC). Before light irradiation, this was done by adding 25 mg of catalyst to TC solution (50 mL, 10 mg/L) and dark stirring for 60 min. The 3 mL suspension was drawn at a spacing interval and the supernatant was centrifugally derived in the course of the experiment. The concentration of TC in the supernatant was determined with UV-visible spectra photometer (P9, Shanghai Mapada Instrument). The characteristic absorption peak of TC is 357 nm.

2.4. Characterization

The X-ray diffraction (XRD) spectra of the powder were recorded on D8 Advance diffractometer. Scanning electron microscopy (SEM, Regulus 8100, Hitachi) was used to observe the shape of powders in secondary electron mode. A Cary 5000 UV-VIS-NIR spectrophotometer (Agilent Technologies, USA) was used to record UV-visible diffuse reflection spectroscopy (UV-Vis DRS) to obtain band-gap energy. X-ray photoelectron spectroscopy (XPS) with $\text{Al K}\alpha$ rays ($h\nu = 1486.6 \text{ eV}$) as excitation source was used for elemental analysis at room temperature. The binding energy was calibrated by adsorbed carbon (284.8 eV), and the peak area of the element was measured by semi-quantitative atomic ratio. The Raman microscope spectroscope (Raman, Renishaw in Via, UK) has recorded Raman spectrum samples with visible light at 532 nm.

2.5. Chemical mechanical polishing experiment

The self-made $\text{Ce}_{1-x}\text{Y}_x\text{Pr}_x\text{O}_2$ abrasives were mixed in deionized water with a planetary ball mill, and were ground for 8 h at the speed of 390 r/min. After complete dispersion, the solid content was adjusted to 0.5 wt% with deionized water. The pH was diluted to 6.0 by NH_4OH solution and HNO_3 solution. Before the CMP experiment began, the polishing slurry was stirred evenly with a magnetic stirrer. The quartz glass used in this experiment was purchased from Lianyungang Xiongtai

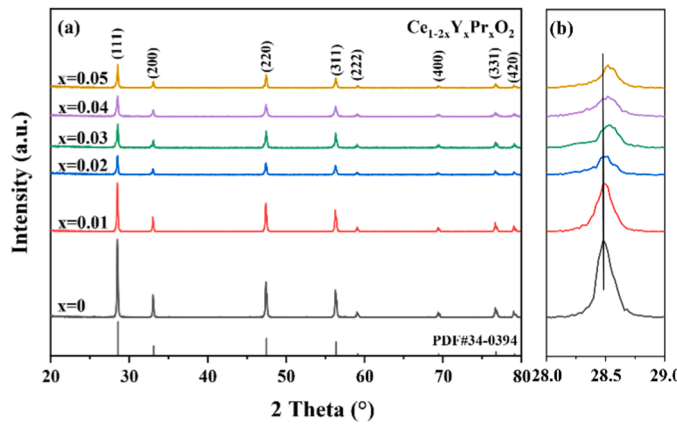


Fig. 2. XRD pattern of $\text{Ce}_{1-2x}\text{Y}_x\text{Pr}_x\text{O}_2$ samples in (a) full range and (b) certain range of fine scanning.

Quartz Technology Co., LTD., with a thickness of 2 mm and a diameter of 20 mm. The automatic pressure grinding and polishing model used in the CMP experiment is UNIPOL-1200S, which was purchased from China Shenyang Kejing Automobile Instrument Co., LTD. Synthetic leather polishing pad is purchased from Shenyang Kejing Automobile Instrument Co., LTD., China. The polishing parameters were set to: the rotational speed of the polishing head was 80 r/min, the antistrophic speed of the polishing platform was 80 r/min, the total time of each polishing was 180 s, the flow rate of the polishing slurry was constant 25 mL/min, and the maximum loading force exerted by the polishing head was 3.5 kg.

The polished quartz glass was washed and dried repeatedly by washing combined with ultrasonic cleaning, and the properties of CMP were characterized. Seiko Instruments Inc. (AFM) was applied to survey the surface morphology of quartz glass and test its roughness at a scanning area of $5 \mu\text{m} \times 5 \mu\text{m}$. The scanning mode was contact mode and the scanning rate was 1.0 Hz. The weight of the polished quartz glass was surveyed by using a precision electronic balance with an accuracy of 0.0001 g. The removal rate (RR , nm/min) used to characterize the polishing efficiency was calculated by Eq. (1) below [49]:

$$RR = \frac{m_2 - m_1}{\rho At} \quad (1)$$

where m_1 and m_2 are respectively the weight of the quartz glass after and before chemical mechanical polishing, ρ is the density of the quartz glass used in this experiment (2.2 g/cm^3), t is the polishing time (180 s), and A is the area of the polished surface of the quartz glass (3.14 cm^2). In this experiment, the final RR is the average of the three repeated experiments.

3. Results and discussion

The XRD pattern of $\text{Ce}_{1-2x}\text{Y}_x\text{Pr}_x\text{O}_2$ samples is shown in Fig. 2. The diffraction peaks of $\text{Ce}_{1-2x}\text{Y}_x\text{Pr}_x\text{O}_2$ samples were well matched with CeO_2 with cubic fluorite structure (JCPDS 34–0394). The peak positions are 28.5° , 33.0° , 47.4° , 56.3° , 59.0° , 69.4° , 76.7° and 79.0° , corresponding to the characteristic peaks of the (111), (200), (220), (311), (222), (400), (331) and (420) planes of the CeO_2 crystal, respectively [50,51]. And there were no other oxides (Ce_2O_3 , Y_2O_3 , Pr_2O_3 , etc.). It indicated that Y^{3+} and Pr^{3+} are effectively doped in CeO_2 lattice, which formed Ce-Y-Pr-O solid solution [40]. With the increase of doping amount, the diffraction peak of (111) crystal plane was shifted to high angle, which was related to lattice shrinkage. In addition, the half-peak width of the diffraction peak became wider after the introduction of Y^{3+} and Pr^{3+} , which indicated that the grain size of CeO_2 crystal decreases. This was consistent with the trend of size change shown in the following SEM images.

In ultra-precision polishing, the shape and size of the abrasive have a great influence on the basic friction behavior and mechanical performance [52]. Fig. 3 are SEM images and grain size profiles of $\text{Ce}_{1-2x}\text{Y}_x\text{Pr}_x\text{O}_2$ samples, respectively. The morphology of samples prepared by different co-doping concentrations showed no significant difference in octahedral shape. It can be seen that the particle size distribution of $\text{Ce}_{0.96}\text{Y}_{0.02}\text{Pr}_{0.02}\text{O}_2$ abrasives were relatively more uniform from the particle size distribution diagrams. The average particle size of $\text{Ce}_{1-2x}\text{Y}_x\text{Pr}_x\text{O}_2$ abrasives was decreased from $\sim 260.36 \text{ nm}$ to $\sim 197.65 \text{ nm}$ with the increase of doping amount of Y^{3+} and Pr^{3+} . The reason for such changes may be due to the electrostatic repulsion between particles and lattice distortion caused by co-doping strategy, which can obstruct the crystal growth [53].

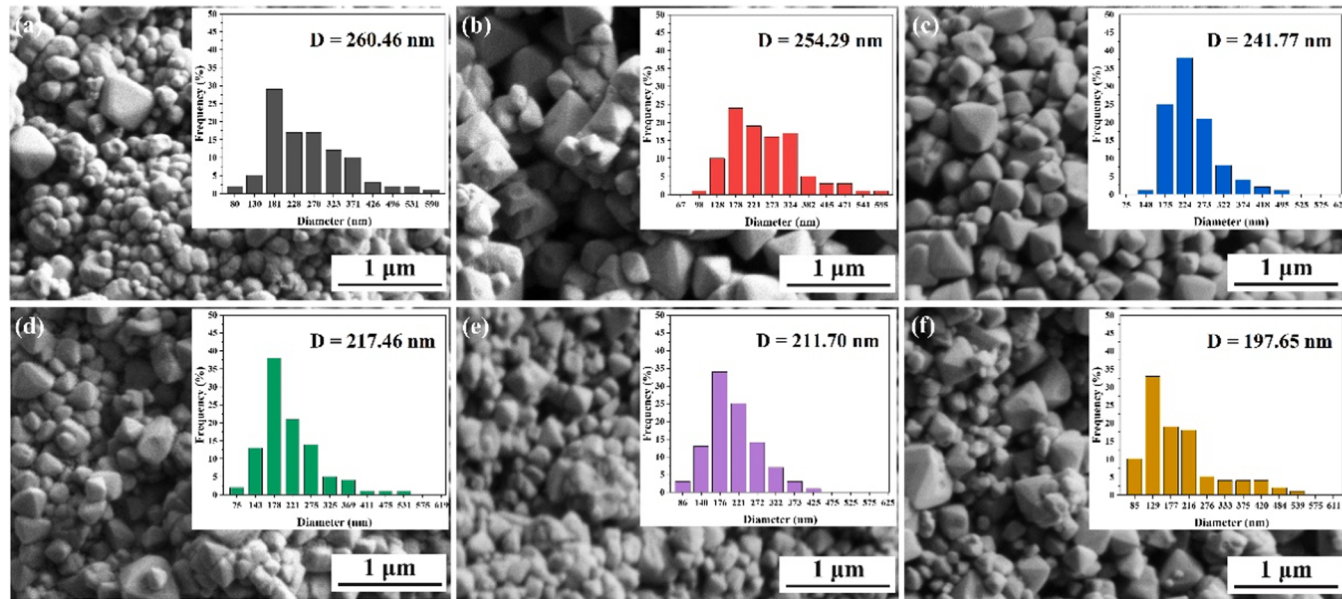


Fig. 3. SEM images and grain size profiles of $\text{Ce}_{1-2x}\text{Y}_x\text{Pr}_x\text{O}_2$ samples. ((a) CeO_2 ; (b) $\text{Ce}_{0.98}\text{Y}_{0.01}\text{Pr}_{0.01}\text{O}_2$; (c) $\text{Ce}_{0.96}\text{Y}_{0.02}\text{Pr}_{0.02}\text{O}_2$; (d) $\text{Ce}_{0.94}\text{Y}_{0.03}\text{Pr}_{0.03}\text{O}_2$; (e) $\text{Ce}_{0.92}\text{Y}_{0.04}\text{Pr}_{0.04}\text{O}_2$; (f) $\text{Ce}_{0.90}\text{Y}_{0.05}\text{Pr}_{0.05}\text{O}_2$).

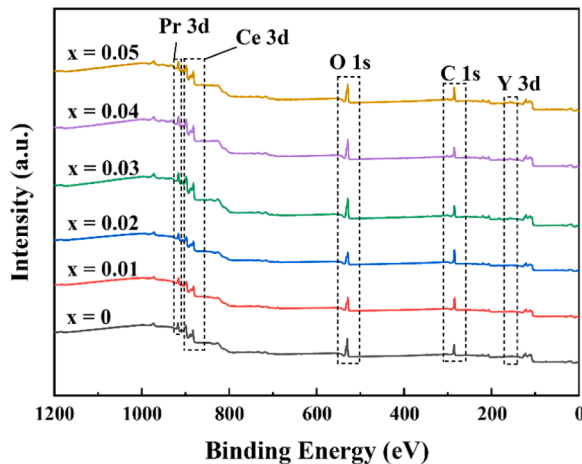


Fig. 4. Wide survey XPS spectrum of $\text{Ce}_{1-2x}\text{Y}_x\text{Pr}_x\text{O}_2$ samples (b-f).

X-ray photoelectron spectroscopy (XPS) is a classically analytical method to identify the composition and chemical state on the materials' surface by measuring the excited photoelectron energy [54–59]. It is used to study the chemical state and element content of the sample. The samples' XPS spectrum are shown in Fig. 4. The spectrum show that only Ce, Y, C and O elements are identified in the samples, while K, Na and Cl elements do not exist, which also manifested that $\text{Ce}_{1-2x}\text{Y}_x\text{Pr}_x\text{O}_2$ is monophasic synthesis. A large number of studies [54, 55, 58–60] have indicated that the cerium dioxide's chemical activity was bound up with Ce^{3+} concentration and oxygen vacancy concentration. Hence, the characteristic spectra of Ce 3d was analyzed in detail. Generally, the spin orbits $3d_{5/2}$ and $3d_{3/2}$ were signed with v and u , respectively. The characteristic peaks of Ce^{3+} were the peaks of v_0 , v' , u_0 and u' , and the peaks of v , v'' , v''' , u , u'' and u''' are assigned to Ce^{4+} . Therefore, with the nonlinear peak fitting method, the peaks of Ce^{3+} and Ce^{4+} were identified, as shown in Fig. 5(a)-(f).

Table 1 shows the peak area data and binding energy of $\text{Ce}_{1-2x}\text{Y}_x\text{Pr}_x\text{O}_2$ samples in diverse valence states of cerium. The concentration of Ce^{3+} can be calculated by Eq. (2), and the integrated peak

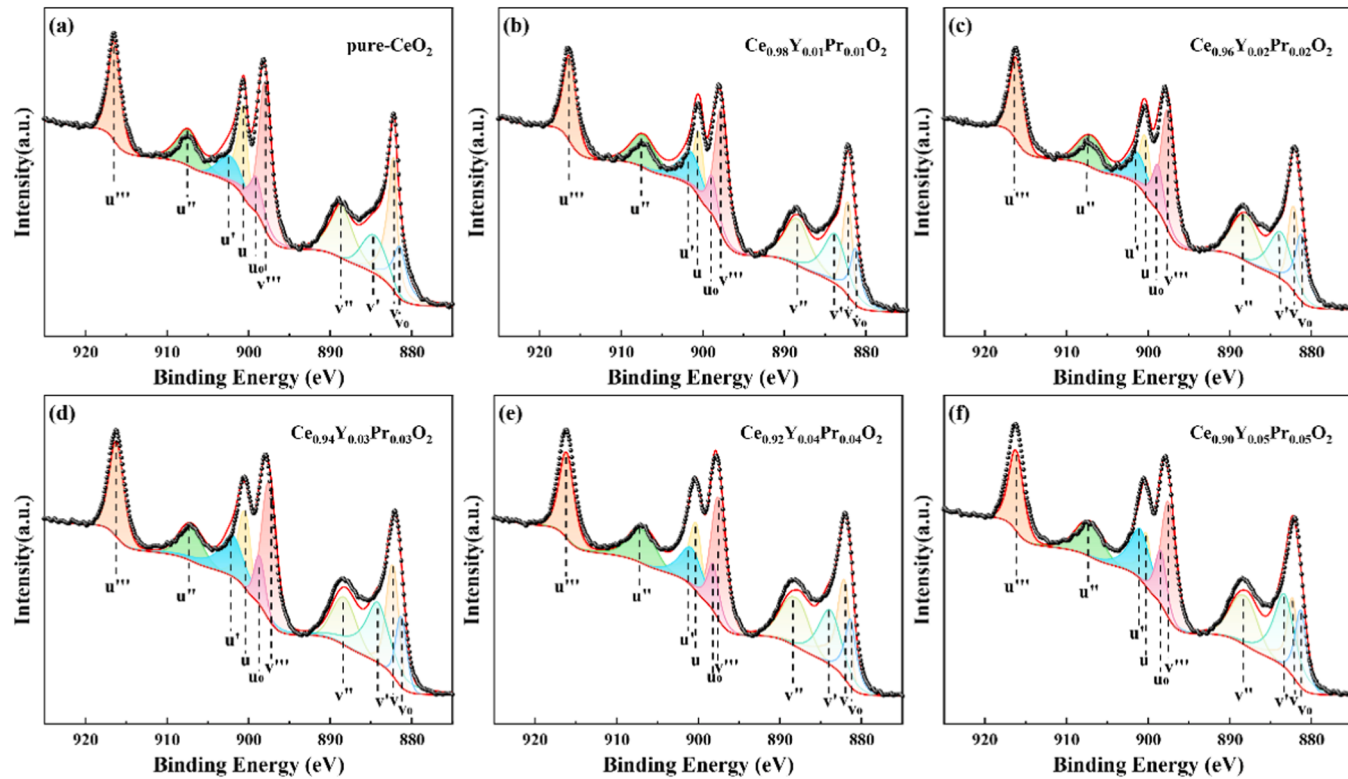


Fig. 5. XPS spectra of Ce 3d for $\text{Ce}_{1-2x}\text{Y}_x\text{Pr}_x\text{O}_2$ samples (a-f).

Table 1

Peak areas and binding energies representing diverse cerium states in $\text{Ce}_{1-2x}\text{Y}_x\text{Pr}_x\text{O}_2$ samples.

		v_0	v	v'	v''	v'''	u_0	u	u'	u''	u'''	Ce^{3+}
x = 0	BE (eV)	881.46	882.17	884.58	888.60	897.94	899.06	900.55	902.18	907.42	916.42	33.55
	Area (%)	7.01	12.11	6.50	9.41	13.97	7.36	12.63	6.74	9.77	14.51	
x = 0.01	BE (eV)	881.25	882.15	883.78	888.29	897.68	898.85	900.43	901.38	907.19	916.24	35.08
	Area (%)	6.69	7.51	10.66	10.41	14.22	6.88	7.65	10.85	10.62	14.50	
x = 0.02	BE (eV)	881.16	882.09	883.75	888.03	897.53	898.73	900.33	901.35	906.93	916.12	36.73
	Area (%)	8.83	7.36	9.32	9.91	14.06	9.09	7.50	9.49	10.10	14.33	
x = 0.03	BE (eV)	881.25	882.23	884.18	888.26	897.46	898.62	900.39	901.96	907.12	916.15	37.25
	Area (%)	5.12	9.67	13.23	7.52	13.93	5.21	9.75	13.69	7.67	14.20	
x = 0.04	BE (eV)	881.47	882.26	883.99	887.92	897.35	898.14	900.79	900.33	906.64	916.08	38.64
	Area (%)	7.40	8.69	11.76	10.30	11.71	7.52	7.63	8.85	9.87	11.94	
x = 0.05	BE (eV)	881.20	882.27	883.29	888.07	897.45	898.38	900.24	900.94	907.02	916.15	39.94
	Area (%)	6.86	7.05	12.93	9.80	12.90	6.98	7.18	13.17	9.99	13.15	

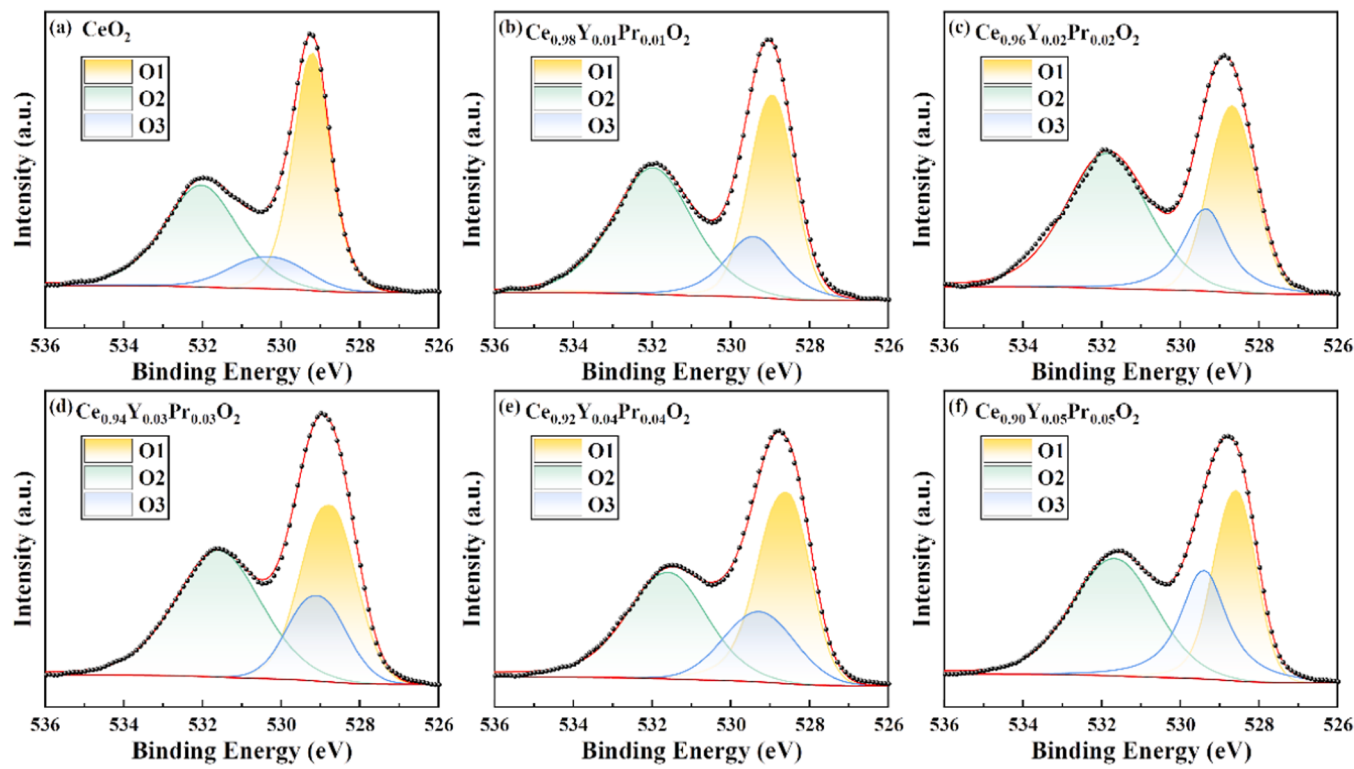
Fig. 6. XPS spectra of O 1 s for $\text{Ce}_{1-2x}\text{Y}_x\text{Pr}_x\text{O}_2$ samples (a-f).

Table 2

Peak areas and binding energies representing diverse oxygen states in $\text{Ce}_{1-2x}\text{Y}_x\text{Pr}_x\text{O}_2$ samples.

		O1	O2	O3	Vo
$x = 0$	BE (eV)	529.17	532.02	530.27	
	Area (%)	45.66	41.21	13.13	13.13
$x = 0.01$	BE (eV)	528.94	531.97	529.39	
	Area (%)	40.57	43.69	15.75	15.75
$x = 0.02$	BE (eV)	528.68	531.86	529.32	
	Area (%)	33.95	48.94	17.10	17.10
$x = 0.03$	BE (eV)	528.75	531.59	529.06	
	Area (%)	36.30	45.34	18.36	18.36
$x = 0.04$	BE (eV)	528.56	531.58	529.61	
	Area (%)	39.89	40.79	19.32	19.32
$x = 0.05$	BE (eV)	528.58	531.68	529.37	
	Area (%)	32.48	43.70	23.82	23.82

area was used for semi-quantitative analysis. It was calculated that the concentration of Ce^{3+} is higher in the $\text{Ce}_{0.96}\text{Y}_{0.02}\text{Pr}_{0.02}\text{O}_2$ abrasive.

$$\frac{C_{(\text{Ce}^{3+})}}{C_{(\text{Ce}^{3+})} + C_{(\text{Ce}^{4+})}} = \frac{\text{area}(v_0 + v' + u_0 + u')}{\text{total area}} \quad (2)$$

Fig. 6 shows the XPS spectrum of O 1 s, and they can be matched with three peaks [53,60,61]. The peaks of O1, O2 and O3 were lattice oxygen, surface adsorbed oxygen and vacancy adsorbed oxygen respectively. The samples' oxygen vacancy (Vo) concentration can be obtained by calculating a ratio that is the ratio of the area of peak O3 to the sum of the areas of all samples' peaks. Table 2 shows the peak area data and binding energy of $\text{Ce}_{1-2x}\text{Y}_x\text{Pr}_x\text{O}_2$ samples in diverse valence states of oxygen. The oxygen vacancy concentration of all samples synthesized in this study was sorted as follows: $\text{Ce}_{0.90}\text{Y}_{0.05}\text{Pr}_{0.05}\text{O}_2$ (23.82%) > $\text{Ce}_{0.92}\text{Y}_{0.04}\text{Pr}_{0.04}\text{O}_2$ (19.32%) > $\text{Ce}_{0.94}\text{Y}_{0.03}\text{Pr}_{0.03}\text{O}_2$ (18.36%) > $\text{Ce}_{0.96}\text{Y}_{0.02}\text{Pr}_{0.02}\text{O}_2$ (17.10%) > $\text{Ce}_{0.98}\text{Y}_{0.01}\text{Pr}_{0.01}\text{O}_2$ (15.75%) > CeO_2 (13.13%). The concentrations of Ce^{3+} and Vo both increase with the increase of doping amount, as shown in Fig. 7. More Ce^{4+} in the CeO_2

crystal was reduced to Ce^{3+} to satisfy the charge balance due to the increased oxygen vacancy.

Raman spectroscopy is an analytical test method using Raman scattering effect. This method researches the scattering spectra of incident light with various frequencies, and thus obtains the message about molecular rotation and vibration, which is used to the research of molecular structure. Raman characterization provides important analysis for the formation about oxygen vacancy in ceria materials. Fig. 8(a) shows the Raman spectrum of $\text{Ce}_{1-2x}\text{Y}_x\text{Pr}_x\text{O}_2$ sample synthesized in this work. It can be observed that the strongest peak occurs at $\sim 465 \text{ cm}^{-1}$ (denoted as F_{2g}), corresponding to the Raman active vibration mode. This peak is attributable to the oxygen ions' symmetrical stretching in the cerium tetrahedral structure. Thus, the structural symmetry of CeO_2 is maintained. Therefore, if there are any gaps/defects in the structure, the peak will be very sensitive to these [62,63]. The doping of $\text{Y}^{3+}/\text{Pr}^{3+}$ in CeO_2 caused the distortion of the partial symmetry of the oxygen ion in the fluorite structure around the Ce ion, resulting in the formation of oxygen vacancy. The appearance of Raman peaks (denoted as α) around $\sim 560 \text{ cm}^{-1}$ were attributed to the production of external oxygen vacancies caused by charge neutral substitution of other trivalent rare earth cations into the CeO_2 lattice as shown in the illustration in Fig. 8(a). As shown in Fig. 8(b), the I_a/I_{F2g} of all samples synthesized in this study was sorted as follows: $\text{Ce}_{0.90}\text{Y}_{0.05}\text{Pr}_{0.05}\text{O}_2$ (0.61) > $\text{Ce}_{0.92}\text{Y}_{0.04}\text{Pr}_{0.04}\text{O}_2$ (0.40) > $\text{Ce}_{0.94}\text{Y}_{0.03}\text{Pr}_{0.03}\text{O}_2$ (0.31) > $\text{Ce}_{0.96}\text{Y}_{0.02}\text{Pr}_{0.02}\text{O}_2$ (0.22) > $\text{Ce}_{0.98}\text{Y}_{0.01}\text{Pr}_{0.01}\text{O}_2$ (0.11) > CeO_2 (0.03). Interestingly, this was the opposite of the trend in the size of samples. As we discussed earlier, co-doping decreased the size of cerium oxide samples, correspondingly increased the specific surface area, and the number of oxygen vacancy defects on the surface were increased, which was consistent with XPS test results.

Uv-vis spectroscopy is often applied to acquire the oxidation state information of metal oxides. The valence state information of Ce element in $\text{Ce}_{1-2x}\text{Y}_x\text{Pr}_x\text{O}_2$ abrasives was preliminatively analyzed using UV-vis DRS diagram. As shown in Fig. 9(a), the absorption peak was Ce^{3+} at the wavelength near 260 nm and Ce^{4+} at the wavelength near

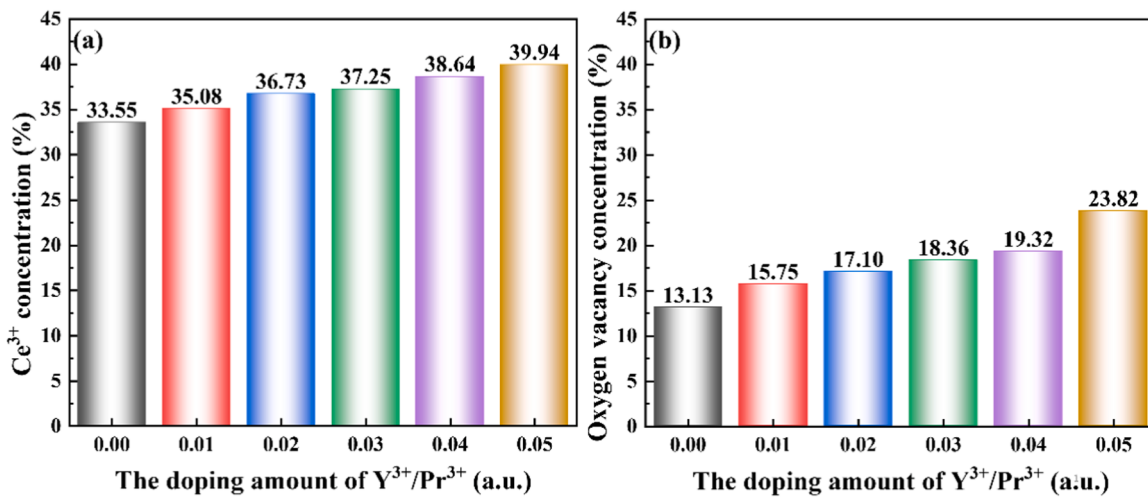


Fig. 7. Ce³⁺ concentration (a) and Oxygen vacancy concentration (b) bar graph for Ce_{1-2x}Y_xPr_xO₂ samples.

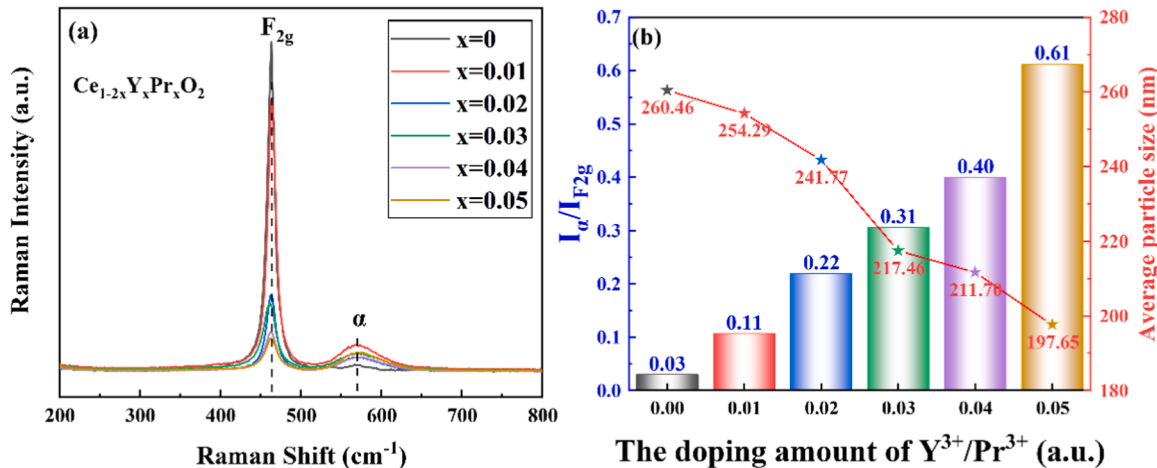


Fig. 8. Raman spectra (a), the I_a/I_{F2g} comparison diagram and average particle size chart (b) of Ce_{1-2x}Y_xPr_xO₂ samples.

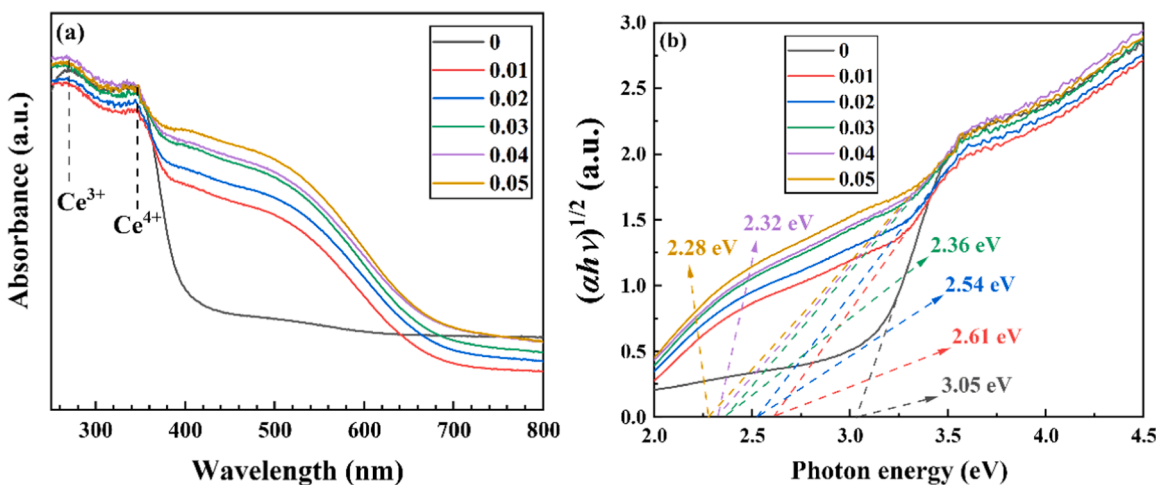


Fig. 9. UV-Vis DRS spectra (a) and Schuster-Kubelka-Munk function (b) of Ce_{1-2x}Y_xPr_xO₂ samples.

340 nm, owing to the electron transition from O 2p level to Ce 4f level. With the increase of doping amount, the optical absorption intensity of the sample increases in the UV range, and the intensity of characteristic peaks belonging to Ce³⁺ and Ce⁴⁺ increases. This can put down to the

increased concentration of oxygen vacancy in the sample. The results showed that co-doping strategy contributed to the increase of Ce³⁺ concentration in abrasives, which had a positive influence on the improvement of abrasive polishing properties. In order to acquire the

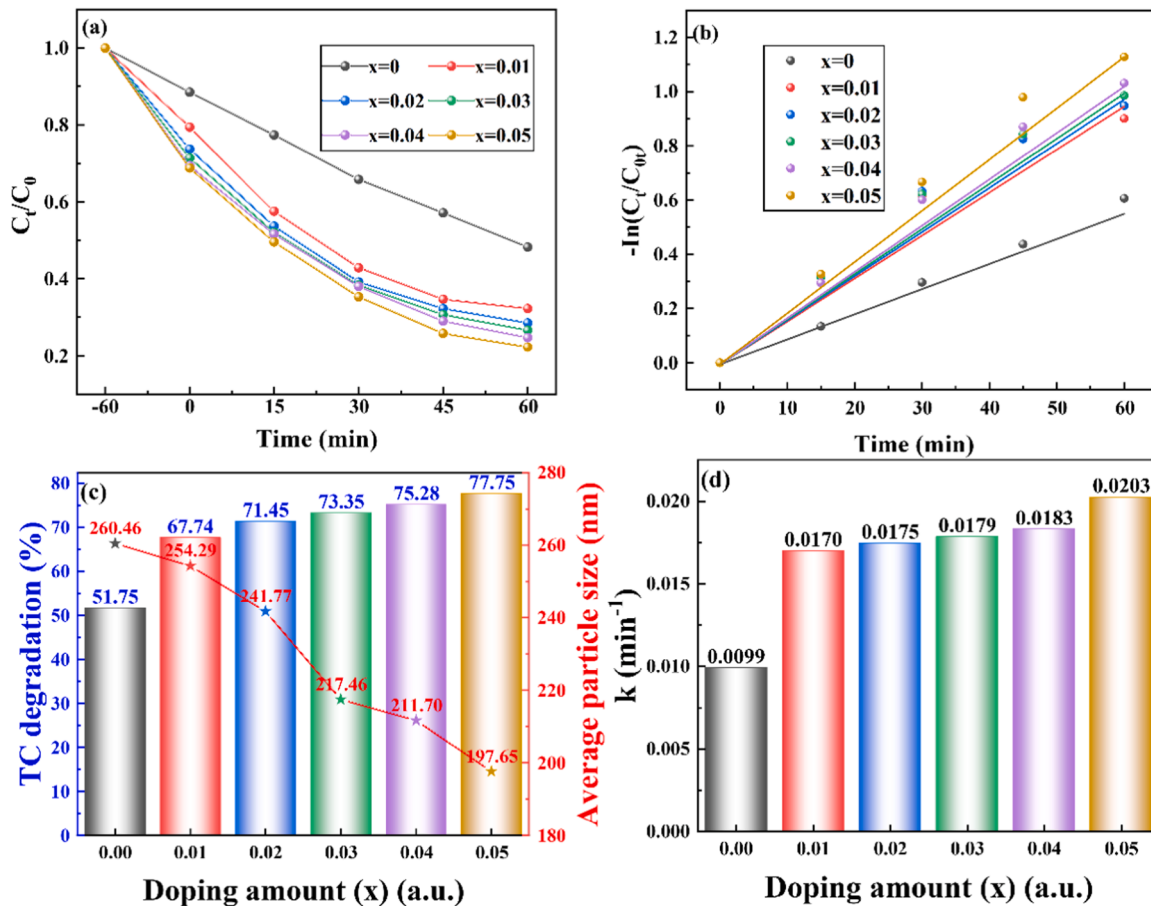


Fig. 10. Photocatalysis efficiency of $\text{Ce}_{1-2x}\text{Y}_x\text{Pr}_x\text{O}_2$ samples for TC photodegradation (a), comparison of photodegradation percentage of TC (c), kinetic curves (b) and comparison of apparent rate constant of diverse photocatalysts (d) for TC photodegradation.

band-gap width (E_g) of $\text{Ce}_{1-2x}\text{Y}_x\text{Pr}_x\text{O}_2$ samples, Schuster-Kubelka-Munk absorption function ($\alpha h\nu$) and photon energy ($h\nu$) were plotted as follows according to Eq. (3):

$$(\alpha h\nu)^n = K (h\nu - E_g) \quad (3)$$

Where ν is the vibration frequency, h is Planck's constant, α is the absorption coefficient, $h\nu$ is the photon energy, and K is the proportionality constant. The type of semiconductor determines the value of n . CeO_2 is the indirect transition semiconductor, so n is equal to 1/2. The rough band gap can be calibrated by measuring the X-intercept of the line, as shown in Fig. 9(b). The E_g of $\text{Ce}_{1-2x}\text{Y}_x\text{Pr}_x\text{O}_2$ ($x = 0.01, 0.02, 0.03, 0.04, 0.05$) samples were equal to 2.61 eV, 2.54 eV, 2.36 eV, 2.32 eV and 2.28 eV, respectively. The $\text{Ce}_{1-2x}\text{Y}_x\text{Pr}_x\text{O}_2$ samples' band gap was narrowed in different degrees compared with the undoped CeO_2 ($E_g = 3.05$ eV), which shows that the photocatalytic activity of the sample promotes by the growth of $\text{Y}^{3+}/\text{Pr}^{3+}$ co-doping amount.

The photocatalytic performance of $\text{Ce}_{1-2x}\text{Y}_x\text{Pr}_x\text{O}_2$ abrasives was characterized with the photocatalytic degradation of tetracycline TC. Fig. 10(a-d) shows the TC degradation curve and its pseudo-first-order kinetic curve. Before the photocatalytic experiment, dark adsorption was carried out for 60 min, so as to avert the influence of particle surface attach on TC degradation performance, and then ultraviolet irradiation was carried out. As shown in Fig. 10(a) and (c), after ultraviolet irradiation for 60 min, the photodegradation efficiency of TC solution was calculated as $\text{Ce}_{0.90}\text{Y}_{0.05}\text{Pr}_{0.05}\text{O}_2$ (77.75%) > $\text{Ce}_{0.92}\text{Y}_{0.04}\text{Pr}_{0.04}\text{O}_2$ (75.28%) > $\text{Ce}_{0.94}\text{Y}_{0.03}\text{Pr}_{0.03}\text{O}_2$ (73.35%) > $\text{Ce}_{0.96}\text{Y}_{0.02}\text{Pr}_{0.02}\text{O}_2$ (71.45%) > $\text{Ce}_{0.98}\text{Y}_{0.01}\text{Pr}_{0.01}\text{O}_2$ (67.74%). The reaction kinetic constants of TC photodegradation process can be computed as follows (4):

$$kt = -\ln\left(\frac{C_t}{C_0}\right) \quad (4)$$

Where, k , t , C_0 and C_t are respectively the reaction kinetic constant, light irradiation time, initial concentration after dark adsorption and residual concentration under a certain irradiation time. As shown as Fig. 10(b) and (d), the k of the calculated samples was as follows: $\text{Ce}_{0.90}\text{Y}_{0.05}\text{Pr}_{0.05}\text{O}_2$ (0.0203 min^{-1}) > $\text{Ce}_{0.92}\text{Y}_{0.04}\text{Pr}_{0.04}\text{O}_2$ (0.0183 min^{-1}) > $\text{Ce}_{0.94}\text{Y}_{0.03}\text{Pr}_{0.03}\text{O}_2$ (0.0179 min^{-1}) > $\text{Ce}_{0.96}\text{Y}_{0.02}\text{Pr}_{0.02}\text{O}_2$ (0.0175 min^{-1}) > $\text{Ce}_{0.98}\text{Y}_{0.01}\text{Pr}_{0.01}\text{O}_2$ (0.0170 min^{-1}) > CeO_2 (0.0099 min^{-1}). The size of the cerium oxide sample was reduced, which increased the specific surface area and the photocatalytic active site. This ultimately allowed the photodegradation capacity of the cerium oxide photocatalyst to be improved by the co-doping strategy, which was the same as the results shown in the former UV-VIS spectrophotometer (Fig. 9).

The surface roughness of the material to be polished is one of the momentous parameters to estimate the polishing performance of the polishing slurry. Fig. 11(a)-(f) is the characterization of two-dimensional (2D) surface morphology of polished matrix after PCMP under atomic force microscopy, where the bright area represents the peak and the dark area represents the valley. Subsequently, the line profile roughness of the diagonal selection area in Fig. 11(a)-(f) was measured. As shown in Fig. 11(g), where the X-axis represents the length of the line profile and the Z-axis represents the depth of the line profile. The improvement of surface quality can be demonstrated by the reduction of line profile roughness. It can be seen that the rough peak and valley distribution of the polished surface of all quartz glass is more uniform than that of the unpolished original quartz glass surface, helping to improve the overall

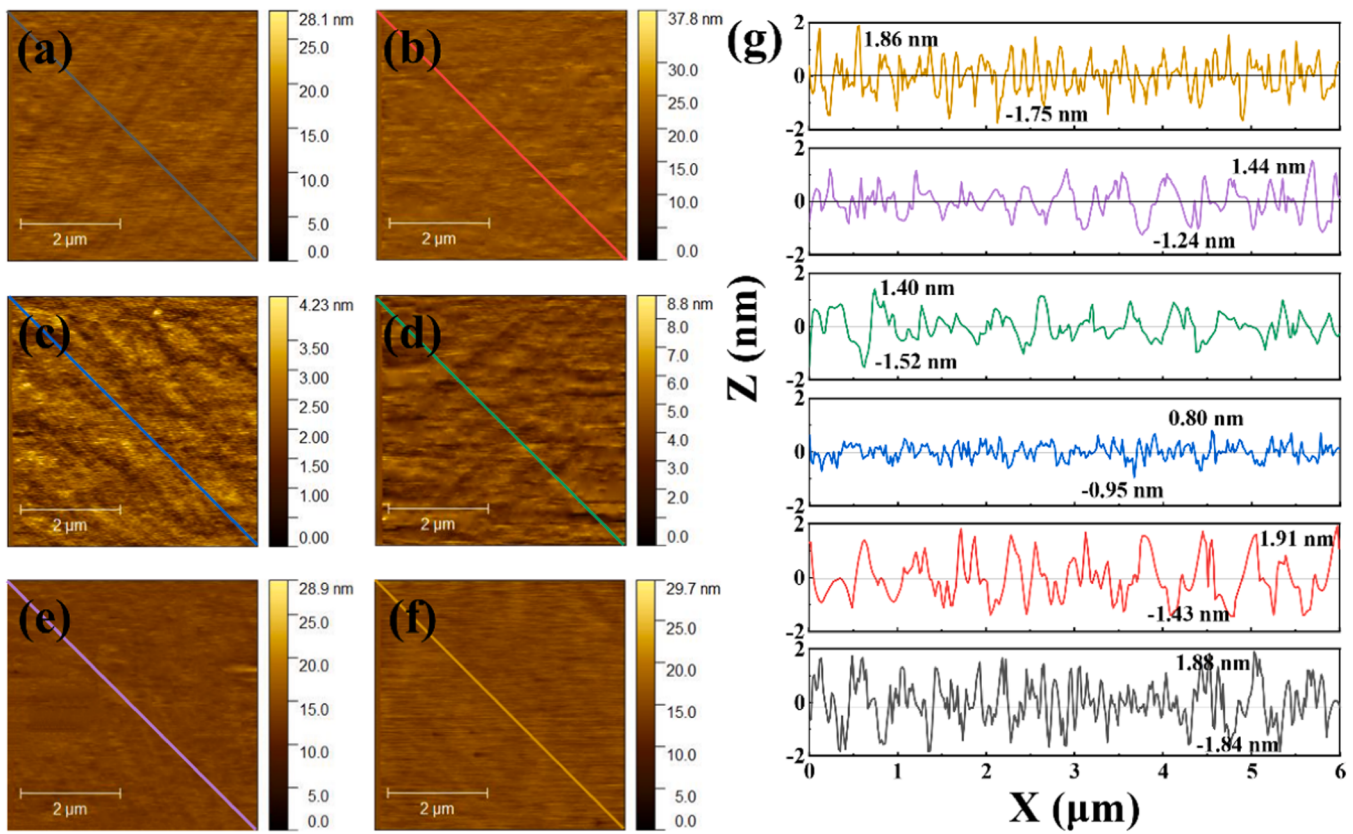


Fig. 11. AFM images of the surface of the quartz glass: after PCMP with (a) CeO_2 , (b) $\text{Ce}_{0.98}\text{Y}_{0.01}\text{Pr}_{0.01}\text{O}_2$, (c) $\text{Ce}_{0.96}\text{Y}_{0.02}\text{Pr}_{0.02}\text{O}_2$, (d) $\text{Ce}_{0.94}\text{Y}_{0.03}\text{Pr}_{0.03}\text{O}_2$, (e) $\text{Ce}_{0.92}\text{Y}_{0.04}\text{Pr}_{0.04}\text{O}_2$ and (f) $\text{Ce}_{0.90}\text{Y}_{0.05}\text{Pr}_{0.05}\text{O}_2$; (g) The corresponding contour line curve.

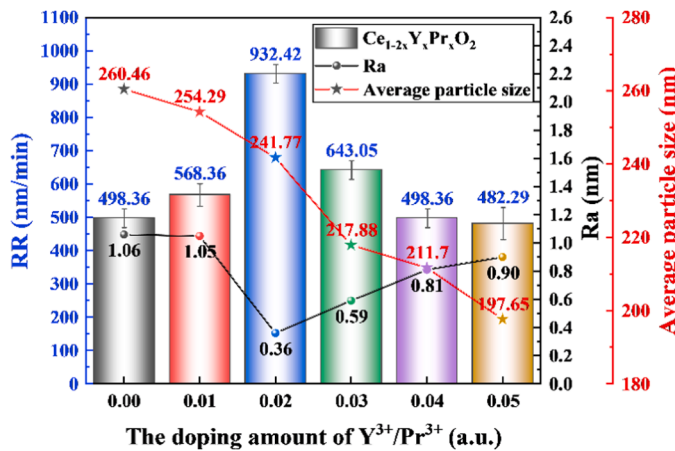


Fig. 12. The surface roughness and removal rate curve of $\text{Ce}_{1-2x}\text{Y}_x\text{Pr}_x\text{O}_2$ samples ($x = 0.00, 0.01, 0.02, 0.03, 0.04, 0.05$).

surface quality. The graph in Fig. 12 showed the average surface roughness (R_a) of the polished quartz glass. The initial roughness of quartz glass was 1.08 nm. The surface quality of the polished matrix was greatly improved by applying the polishing slurry containing $\text{Ce}_{1-2x}\text{Y}_x\text{Pr}_x\text{O}_2$, and the surface roughness was memorably reduced compared with the control group. The introduction of Y^{3+} and Pr^{3+} reduced the R_a of polished quartz glass. With the further increase of doping amount, the roughness increased slightly. Among them, the R_a of polishing slurry prepared with $\text{Ce}_{0.96}\text{Y}_{0.02}\text{Pr}_{0.02}\text{O}_2$ abrasive was 0.36 nm. The specific reasons will be discussed later in the mechanism section.

The Removal rate (RR) of the material is also a significant index to

appraise the polishing properties of polishing slurry. The bar chart in Fig. 12 represents the RR of quartz glass after $\text{Ce}_{1-2x}\text{Y}_x\text{Pr}_x\text{O}_2$ nanoparticle polishing. Co-doping strategy increased the RR of PCMP and decreased with further increase of doping amount. When the doping amount was 0.02, the RR of the abrasive was 932.42 nm/min. The change of abrasive RR was mainly the synergistic effect of Ce^{3+} concentration and particle size. When the doping amount was 0.02, Ce^{3+} concentration and particle size reached a dynamic equilibrium in the research system of this experiment, thus making RR reach the best in this work. Combined with the previous test results, we can conclude that in this work, the prepared $\text{Ce}_{1-2x}\text{Y}_x\text{Pr}_x\text{O}_2$ abrasive has the best PCMP performance when the single doping amount was 0.02.

Cook [64] proposed that chemical-mechanical polishing is the grinding of the surface of the material due to the mechanical action of abrasive particles pressed into the surface of the workpiece along with the flow of polishing fluid (Fig. 13 (a)), and is coordinated with chemical action to achieve the purpose of material removal. Fig. 13 shows the PCMP mechanism of $\text{Ce}_{1-2x}\text{Y}_x\text{Pr}_x\text{O}_2$ abrasive on quartz glass. In this study, the co-doping of Y^{3+} and Pr^{3+} increased the content of Ce^{3+} on the surface of samples, reduced the band gap of $\text{Ce}_{1-2x}\text{Y}_x\text{Pr}_x\text{O}_2$, enhanced the photocatalytic activity of abrasives, and further improved the material removal rate of abrasives, as can be seen in illustration (c) of Fig. 13 (b).

Under light irradiation, electrons transition from the valence band to the conduction band, producing e^-/h^+ . In PCMP, $\text{Ce}_{1-2x}\text{Y}_x\text{Pr}_x\text{O}_2$ samples absorb ultraviolet radiation to produce photogenerated charge carriers. $\text{Y}^{3+}/\text{Pr}^{3+}$ co-doping narrowed the band gap of CeO_2 to 2.28 eV (E_g of pure CeO_2 synthesized in this experiment was 3.05 eV), and the photogenerated electron (e^-) was more likely to transition from valence band (VB) to conduction band (CB) after excitation, resulting in oxidation site (h^+) in VB and reduction site (e^-) in CB. Form a photogenerated electron-hole pair (e^-/h^+) [65], as can be seen in illustration (c) of

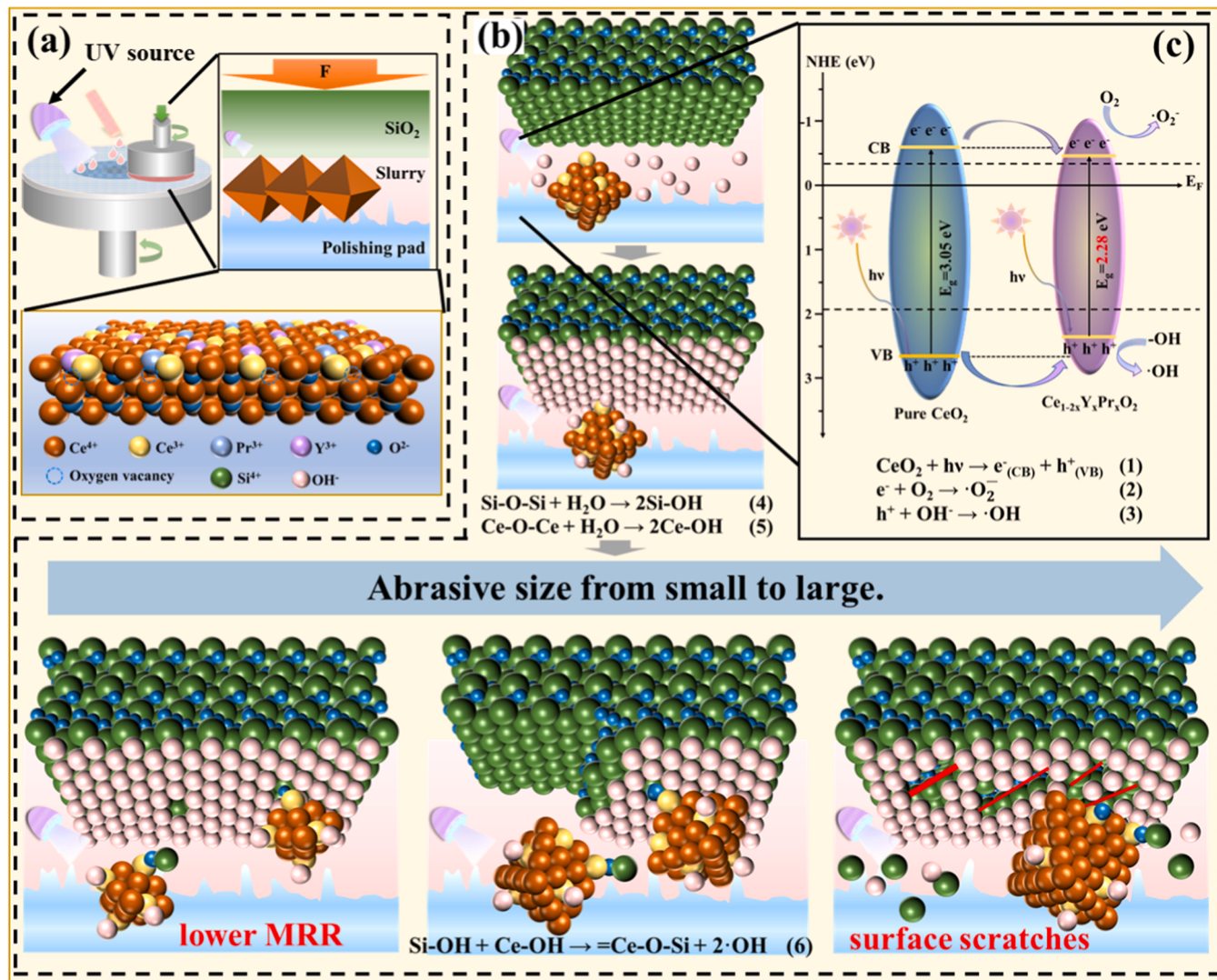


Fig. 13. PCMP mechanism diagram of $\text{Ce}_{1-x}\text{Y}_x\text{Pr}_x\text{O}_2$ samples.

Fig. 13 (b). The photo-biogenic carrier can react with the surrounding medium to form oxidizing active groups, such as superoxide free radicals ($\cdot\text{O}_2^-$), hydroxyl free radicals ($\cdot\text{OH}$), h^+ , etc. These oxidizing active groups leads to better degradation of materials [65]. Y^{3+} and Pr^{3+} will produce impurity levels in the CeO_2 gap, which will reduce the gap width. The purpose of this strategy is to form a receptor layer below CB of CeO_2 to facilitate the downward flow of electrons from CeO_2 CB to the doping layer, thereby inhibiting the recombination of photogenerated carriers. After doping Y^{3+} and Pr^{3+} in the CeO_2 lattice, we reason, the exposed Ce^{4+} portion is replaced by Y^{3+} and Pr^{3+} . The oxygen vacancy can efficiently trap electrons in CB and limit the rate of photogenerated carrier recombination in $\text{Ce}_{1-x}\text{Y}_x\text{Pr}_x\text{O}_2$, as shown by chemical Eqs. (1)–(3) in the Fig. 13 (b). Therefore, $\text{Ce}_{1-x}\text{Y}_x\text{Pr}_x\text{O}_2$ samples have good photocatalytic activity.

SiO_2 substrate and $\cdot\text{OH}$ in the polishing slurry contact and hydration reaction occurs, Si-OH bond is formed on the surface of SiO_2 substrate, and $\text{Si}(\text{OH})_4$ hydration layer is generated, as shown by chemical Eq. (4) in the Fig. 13 (b) [6]. These active substances in the polish are thought to provide additional strong oxidation activity, which accelerates the production of chemical reaction layers. It is generally believed that the increase in the chemical reactivity of the slurry helps the surface of the quartz glass to be polished, forming a hydration layer that is faster and easier to remove, thus improving RR [40]. At the same time, the surface of CeO_2 is dissociated by H_2O to form an $\cdot\text{OH}$ group, and silicate ions are

adsorbed to the surface of CeO_2 through the interaction with the $\cdot\text{OH}$ group, as shown by chemical equation (5) in the Fig. 13 (b). The chemistry of the material removal process in SiO_2 chemical-mechanical polishing depends on the interaction between the SiO_2 layer and samples on the surface and the water and chemical agent in the polishing slurry [64].

In this study, Ce^{3+} ions can be used as the active site on the surface of cerium oxide and react with the glass surface to form Ce-O-Si bonds, as shown by chemical equation (6) in the Fig. 13 (b). The new bond is stronger than the Si-O-Si bond on the surface of molten silica. Under the action of the mechanical force applied by the polishing machine. Si-O-Si bond is broken. Remove the polished quartz glass surface. In the case of polishing silica, it is generally believed that the high concentration of Ce^{3+} on the surface of CeO_2 abrasive is the reason for its high reactivity with the SiO_2 matrix. It was covered in literature [29, 33, 40, 66–72] that CeO_2 abrasives rich in Ce^{3+} obtained significant removal capacity, which may be due to the enhanced tribological chemical activity to the quartz glass (accelerates the becoming of Ce-O-Si bonds). The RR of the prepared $\text{Ce}_{1-x}\text{Y}_x\text{Pr}_x\text{O}_2$ abrasive was obviously improved under PCMP conditions, which may be due to the enhanced photocatalytic activity of $\text{Ce}_{1-x}\text{Y}_x\text{Pr}_x\text{O}_2$ polishing slurry under UV irradiation and the appropriate particle size.

In this work, abrasives with relatively uniform particle size distribution and an average size of around 240 nm exhibit excellent PCMP

properties due to having more active sites. As shown in the bottom half of the Fig. 13 (b), large particle size can promote the improvement of *RR*, but it is not friendly to improve its photocatalytic ability, so the softening layer cannot be quickly generated [42,43,53]. The chemical reaction rate of CeO₂-based particle cannot keep up with the mechanical removal rate. At the same time, due to excessive polishing, the surface of the workpiece to be polished will be scratched and worn, which will affect the surface quality of the material. On the contrary, small particle size can improve the photocatalytic performance, but has no advantage in mechanical removal rate, thus reducing *RR* and increasing time cost.

4. Conclusions

In this work, a series of Ce_{1-2x}Y_xPr_xO₂ abrasives with normal octahedral shape were synthesized and applied to PCMP as functional abrasives. PCMP results show that a smooth surface with low roughness can be obtained. As expected, the grinding rate of Ce_{1-2x}Y_xPr_xO₂ abrasive improved by approximately 87.10% compared to the undoped CeO₂ abrasive. Y/Pr co-doping improved the separation efficiency of the photogenic carrier of CeO₂ particle photocatalyst, and enhanced the photochemical oxidation activity. This further promoted the generation of oxidizing active substances (-OH, ·O₂, h⁺, etc.) in the polishing slurry. Therefore, the formation and removal of chemical reactions in the soft layer are accelerated. The Ce_{1-2x}Y_xPr_xO₂ abrasive prepared in this study had the advantages of reducing surface roughness and increasing removal velocity, and was suitable for various CMP, PCMP, and application fields. This study is well on the way to providing a new approach and experimental basis for the design and synthesis of cerium specialized abrasives.

CRediT authorship contribution statement

Xu Ning: Formal analysis, Funding acquisition, Methodology, Project administration, Resources. **Luo Yuxin:** Data curation, Formal analysis, Investigation, Software, Visualization, Writing - original draft, Writing - review & editing. **Lin Yu:** Validation. **Ma Jiahui:** Validation. **Pu Yongping:** Methodology, Supervision.

Declaration of Competing Interest

The authors declare that they have no known competing financial interests or personal relationships that could have appeared to influence the work reported in this paper.

Data availability

Data will be made available on request.

Acknowledgements

This work was financially supported by General Program of National Natural Science Foundation of China (No. 52373314), the National Natural Science Foundation of China (No. 51905324), the Shaanxi Collaborative Innovation Center of Industrial Auxiliary Chemistry and Technology of Shaanxi University of Science and Technology (No. KFKT2022-09), Key Research and Development Projects of Shaanxi Province (No. 2023-YBGY-499), and the Postdoctoral Science Foundation of China (No. 2022MD713771).

References

- [1] D. Liu, Z. Zhang, H. Zhou, X. Deng, C. Shi, F. Meng, Z. Yu, J. Feng, Angstrom surface on copper induced by novel green chemical mechanical polishing using ceria and silica composite abrasives, *Appl. Surf. Sci.* (2023), <https://doi.org/10.1016/j.apsusc.2023.158382>.
- [2] L. Liu, Z. Zhang, C. Shi, H. Zhou, D. Liu, Y. Li, G. Xu, J. Feng, F. Meng, Atomic surface of fused silica and polishing mechanism interpreted by molecular dynamics and density functional theory, *Mater. Today Sustain.* 23 (2023), <https://doi.org/10.1016/j.mtsust.2023.100457>.
- [3] W. Xie, Z. Zhang, L. Liao, J. Liu, H. Su, S. Wang, D. Guo, Green chemical mechanical polishing of sapphire wafers using a novel slurry, *Nanoscale* 12 (2020) 22518–22526, <https://doi.org/10.1039/d0nr04705h>.
- [4] L. Liao, Z. Zhang, F. Meng, D. Liu, B. Wu, Y. Li, W. Xie, A novel slurry for chemical mechanical polishing of single crystal diamond, *Appl. Surf. Sci.* 564 (2021), <https://doi.org/10.1016/j.apsusc.2021.150431>.
- [5] Z. Zhang, L. Liao, X. Wang, W. Xie, D. Guo, Development of a novel chemical mechanical polishing slurry and its polishing mechanisms on a nickel alloy, *Appl. Surf. Sci.* 506 (2020), <https://doi.org/10.1016/j.apsusc.2019.144670>.
- [6] X. Cui, Z. Zhang, S. Yu, X. Chen, C. Shi, H. Zhou, F. Meng, J. Yu, W. Wen, Unprecedented atomic surface of silicon induced by environmentally friendly chemical mechanical polishing, *Nanoscale* 15 (2023) 9304–9314, <https://doi.org/10.1039/d3nr01149f>.
- [7] J. Liu, Z. Zhang, C. Shi, Z. Ren, J. Feng, H. Zhou, Z. Liu, F. Meng, S. Zhao, Novel green chemical mechanical polishing of fused silica through designing synergistic CeO₂/h-BN abrasives with lubricity, *Appl. Surf. Sci.* 637 (2023), <https://doi.org/10.1016/j.apsusc.2023.157978>.
- [8] D. Liu, Z. Zhang, J. Feng, Z. Yu, F. Meng, C. Shi, G. Xu, S. Shi, W. Liu, Environment-friendly chemical mechanical polishing for copper with atomic surface confirmed by transmission electron microscopy, *Colloids Surf. A: Physicochem. Eng. Asp.* 656 (2023), <https://doi.org/10.1016/j.colsurfa.2022.130500>.
- [9] Y. Li, Z. Zhang, C. Shi, D. Liu, L. Liu, Density functional theory analysis and novel green chemical mechanical polishing for potassium dihydrogen phosphate, *Colloids Surf. A: Physicochem. Eng. Asp.* 662 (2023), <https://doi.org/10.1016/j.colsurfa.2023.131000>.
- [10] A. Chen, T. Wang, Y. Chen, S. Wang, Y. Chen, Development of polystyrene/polyaniline/ceria (PS/PANI/CeO₂) multi-component abrasives for photochemical mechanical polishing/planarization applications, *Appl. Surf. Sci.* 575 (2022), <https://doi.org/10.1016/j.apsusc.2021.151784>.
- [11] Q. Zhao, Z. Sun, B. Guo, Material removal mechanism in ultrasonic vibration assisted polishing of micro cylindrical surface on SiC, *Int. J. Mach. Tools Manuf.* 103 (2016) 28–39, <https://doi.org/10.1016/j.ijmachtools.2016.01.003>.
- [12] N. Sihag, P. Kala, P.M. Pandey, Analysis of surface finish improvement during ultrasonic assisted magnetic abrasive finishing on chemically treated tungsten substrate, *Procedia Manuf.* 10 (2017) 136–146, <https://doi.org/10.1016/j.promfg.2017.07.040>.
- [13] H.P. Wan Hongqiang, Shuai Ge, Fangcong Li, Zhihao Liu, Development of ultrasonic vibration polishing method on workpiece surface, *Diam. Abras. Eng.* 28 (2018).
- [14] R.K. Li Huai, Y.I.N. Zhen, D.A.I. Chenwei, W.A.N.G. Zhongwang, W.E.I. Li, W.E.I. Dong, Review of ultrasonic vibration-assisted abrasive flow polishing technology, *J. Mech. Eng.* 57 (2021), <https://doi.org/10.3901/jme.2021.09.233>.
- [15] T. Yu, T. Zhang, X. Yu, X. Yang, J. Sun, Study on optimization of ultrasonic-vibration-assisted polishing process parameters, *Measurement* 135 (2019) 651–660, <https://doi.org/10.1016/j.measurement.2018.12.008>.
- [16] K. Ding, Y. Fu, H. Su, H. Xu, F. Cui, Q. Li, Experimental studies on matching performance of grinding and vibration parameters in ultrasonic assisted grinding of SiC ceramics, *Int. J. Adv. Manuf. Technol.* 88 (2016) 2527–2535, <https://doi.org/10.1007/s00170-016-8977-6>.
- [17] C.C.N. Ballarina, R. Maboudianb, L. Magagnin, Electropolishing of n-type 3C-polyocrystalline silicon carbide, *Electrochim. Commun.* 40 (2014) 17–19, <https://doi.org/10.1016/j.elecom.2013.12.018>.
- [18] H. Deng, K. Hosoya, Y. Imanishi, K. Endo, K. Yamamura, Electro-chemical mechanical polishing of single-crystal SiC using CeO₂ slurry, *Electrochim. Commun.* 52 (2015) 5–8, <https://doi.org/10.1016/j.elecom.2015.01.002>.
- [19] X. Yang, X. Yang, R. Sun, K. Kawai, K. Arima, K. Yamamura, Obtaining Atomically Smooth 4H-SiC (0001) Surface by Controlling Balance Between Anodizing and Polishing in Electrochemical Mechanical Polishing, *Nanomanufacturing Metrol.* 2 (2019) 140–147, <https://doi.org/10.1007/s41871-019-00043-5>.
- [20] J. Murata, K. Yodogawa, K. Ban, Polishing-pad-free electrochemical mechanical polishing of single-crystalline SiC surfaces using polyurethane-CeO₂ core-shell particles, *Int. J. Mach. Tools Manuf.* 114 (2017) 1–7, <https://doi.org/10.1016/j.ijmachtools.2016.11.007>.
- [21] K. Yamamura, K. Hosoya, Y. Imanishi, H. Deng, K. Endo, Preliminary Study on Highly Efficient Polishing of 4H-SiC by Utilization of Anodic Oxidation, *Adv. Mater. Res.* 1017 (2014) 509–514, <https://doi.org/10.4028/www.scientific.net/AMR.1017.509>.
- [22] D.D. Mahender Kumar Gupta, Inder Mohan Chhabra, Sunil Jha, Buchi Suresh Madireddy, Experimental investigation and machine parameter optimization for nano-finishing of fused silica using magnetorheological finishing process, (2020). <https://doi.org/10.1016/j.ijleo.2020.165908>.
- [23] G. Ghosh, A. Sidpara, P.P. Bandyopadhyay, Magnetorheological finishing of WC-Co coating using iron-B4C-CNT composite abrasives, *Tribology Int.* 155 (2021), <https://doi.org/10.1016/j.triboint.2020.106807>.
- [24] A.S. Rana, T.S. Bedi, V. Grover, Fine-finishing of stepped cylindrical workpiece using magnetorheological finishing process, *Mater. Today.: Proc.* 41 (2021) 886–892, <https://doi.org/10.1016/j.matpr.2020.09.455>.
- [25] S. Liu, H. Wang, Q. Zhang, J. Hou, B. Zhong, X. Chen, Regionalized modeling approach of tool influence function in magnetorheological finishing process for aspherical optics, *Optik* 206 (2020), <https://doi.org/10.1016/j.ijleo.2020.164368>.
- [26] M. Singh, A.K. Singh, Improved magnetorheological finishing process with rectangular core tip for external cylindrical surfaces, *Mater. Manuf. Process.* 34 (2019) 1049–1061, <https://doi.org/10.1080/10426914.2019.1594272>.

- [27] A. Kumar, Z. Alam, D.A. Khan, S. Jha, Nanofinishing of FDM-fabricated components using ball end magnetorheological finishing process, *Mater. Manuf. Process.* 34 (2018) 232–242, <https://doi.org/10.1080/10426914.2018.1512136>.
- [28] M. Singh, A.K. Singh, Theoretical investigations into magnetorheological finishing of external cylindrical surfaces for improved performance, *Proceedings of the Institution of Mechanical Engineers, Part C: J. Mech. Eng. Sci.* 234 (2020) 4872–4892, <https://doi.org/10.1177/0954406220931550>.
- [29] W. Ma, T. Mashimo, S. Tamura, M. Tokuda, S. Yoda, M. Tsushida, M. Koinuma, A. Kubota, H. Isobe, A. Yoshiasa, Cerium oxide ($\text{CeO}_2\text{-x}$) nanoparticles with high Ce^{3+} proportion synthesized by pulsed plasma in liquid, *Ceram. Int.* 46 (2020) 26502–26510, <https://doi.org/10.1016/j.ceramint.2020.07.093>.
- [30] R. Li, Y. Zhang, Y. Zhang, W. Liu, Y. Li, H. Deng, Plasma-based isotropic etching polishing of synthetic quartz, *J. Manuf. Process.* 60 (2020) 447–456, <https://doi.org/10.1016/j.jmapro.2020.10.075>.
- [31] R. Sun, X. Yang, K. Arima, K. Kawai, K. Yamamura, High-quality plasma-assisted polishing of aluminum nitride ceramic, *CIRP Ann.* 69 (2020) 301–304, <https://doi.org/10.1016/j.cirp.2020.04.096>.
- [32] I. Muhammad, H. Warda, S. Muhammad, H.H. Somaily, S.K. Hachim, J.K. Zainab, H.A. Lafta, Y.S. Alnassar, M.R. Ahmed, R.E. Syeda, A. Muhammad, Wet-chemical synthesis of $\text{ZnO}/\text{CdO}/\text{CeO}_2$ heterostructure: a novel material for environmental remediation application, *Ceram. Int.* 48 (2022) 34590–34601, <https://doi.org/10.1016/j.ceramint.2022.08.046>.
- [33] A. Chen, Y. Duan, Z. Mu, W. Cai, Y. Chen, Meso-silica/Erbium-doped ceria binary particles as functionalized abrasives for photochemical mechanical polishing (PCMP), *Appl. Surf. Sci.* 550 (2021), <https://doi.org/10.1016/j.apsusc.2021.149353>.
- [34] Y. He, Z. Yuan, S. Song, X. Gao, W. Deng, Investigation on material removal mechanisms in photocatalysis-assisted chemical mechanical polishing of 4H-SiC wafers, *Int. J. Precis. Eng. Manuf.* 22 (2021) 951–963, <https://doi.org/10.1007/s12541-021-00494-1>.
- [35] T. Munawar, S. Sardar, M.S. Nadeem, F. Mukhtar, S. Manzoor, M.N. Ashiq, S. A. Khan, M. Koc, F. Iqbal, Rational design and electrochemical validation of reduced graphene oxide (rGO) supported $\text{CeO}_2\text{-Nd}_2\text{O}_3\text{/rGO}$ ternary nanocomposite as an efficient material for supercapacitor electrodes, *J. Appl. Electrochem.* 53 (2023) 1853–1868, <https://doi.org/10.1007/s10800-023-01885-0>.
- [36] M.S. Nadeem, T. Munawar, F. Mukhtar, S. Manzoor, K. Mahmood, M.S. Al-Buraihi, K.M. Katubi, M.N. Ashiq, I. Boukhris, F. Iqbal, Facile synthesis of sunlight driven photocatalysts $\text{Zn}_0.9\text{Ho}_0.05\text{M}_0.05\text{O}$ ($\text{M} = \text{Pr}, \text{Sm}, \text{Er}$) for the removal of synthetic dyes from wastewater, *Surf. Interfaces* 34 (2022), <https://doi.org/10.1016/j.surfin.2022.102376>.
- [37] T. Munawar, M. Shahid Nadeem, F. Mukhtar, S. Manzoor, M. Naeem Ashiq, S. Batool, M. Hasan, F. Iqbal, Multifunctional dual Z-scheme heterostructured $\text{Sm}_2\text{O}_3\text{-WO}_3\text{-La}_2\text{O}_3$ nanocomposite: enhanced electrochemical, photocatalytic, and antibacterial properties, *Adv. Powder Technol.* 34 (2023), <https://doi.org/10.1016/j.apert.2023.104061>.
- [38] F. Mukhtar, T. Munawar, M.S. Nadeem, M. Naveed ur Rehman, S.A. Khan, M. Koc, S. Batool, M. Hasan, F. Iqbal, Dual Z-scheme core-shell PANI-CeO₂-Fe2O3-NiO heterostructured nanocomposite for dyes remediation under sunlight and bacterial disinfection, *Environ. Res.* 215 (2022), <https://doi.org/10.1016/j.envres.2022.114140>.
- [39] J. Ma, N. Xu, Y. Luo, Y. Lin, Y. Pu, Enhancing the polishing efficiency of CeO₂ abrasives on the SiO₂ substrates by improving the Ce³⁺ concentration on their surface, *ACS Appl. Electron. Mater.* (2022), <https://doi.org/10.1021/acsaelm.2c01553>.
- [40] Y. Chen, L. Zhong, A. Chen, M. Fu, X. Lu, Highly dispersed Gd-CeO₂ nanocrystals supported on mesoporous silica composite particles towards photochemical (photo-assisted chemical) mechanical polishing, *Ceram. Int.* (2023), <https://doi.org/10.1016/j.ceramint.2023.02.055>.
- [41] R. Schmitt, A. Nenning, O. Kravins, R. Korobko, A.I. Frenkel, I. Lubomirsky, S. M. Haile, J.L.M. Rupp, A review of defect structure and chemistry in ceria and its solid solutions, *Chem. Soc. Rev.* 49 (2020) 554–592, <https://doi.org/10.1039/c9cs00588a>.
- [42] M.A. Majeed Khan, W. Khan, M. Naziruddin Khan, A.N. Alhazaa, Enhanced visible light-driven photocatalytic performance of Zr doped CeO₂ nanoparticles, *J. Mater. Sci.: Mater. Electron.* 30 (2019) 8291–8300, <https://doi.org/10.1007/s10854-019-01147-w>.
- [43] K. Singh, K. Kumar, S. Srivastava, A. Chowdhury, Effect of rare-earth doping in CeO₂ matrix: correlations with structure, catalytic and visible light photocatalytic properties, *Ceram. Int.* 43 (2017) 17041–17047, <https://doi.org/10.1016/j.ceramint.2017.09.116>.
- [44] G. Xu, Z. Zhang, F. Meng, L. Liu, D. Liu, C. Shi, X. Cui, J. Wang, W. Wen, Atomic-scale surface of fused silica induced by chemical mechanical polishing with controlled size spherical ceria abrasives, *J. Manuf. Process.* 85 (2023) 783–792, <https://doi.org/10.1016/j.jmapro.2022.12.008>.
- [45] N. Xu, Y. Luo, J. Ma, Y. Lin, X. Zhu, Y. Pu, Enhancement mechanism of Y-doped $\text{Ce}_1\text{-xYxO}_2$ for photocatalytic-assisted chemical-mechanical polishing, *Mater. Today Commun.* 38 (2024), <https://doi.org/10.1016/j.mtcomm.2023.107791>.
- [46] T. Munawar, S. Fatima, M.S. Nadeem, F. Mukhtar, U.A. Akbar, A.S. Hakeem, F. Iqbal, Tunability of physical properties of NiO by the introduction of rare earth metal (Y, Ho) dual doping for natural sunlight-driven photocatalysis, *J. Mater. Sci.: Mater. Electron.* 34 (2023) 1–24, <https://doi.org/10.1007/s10854-023-10095-5>.
- [47] T. Munawar, S. Manzoor, F. Mukhtar, M.S. Nadeem, A.G. Abid, M.N. Ashiq, F. Iqbal, Facile synthesis of nanosphere like rare-earth/transition metal dual-doped TiO₂ nanostructure for application as supercapacitor electrodes material, *J. Mater. Sci.* 57 (2022) 11852–11870, <https://doi.org/10.1007/s10853-022-07390-7>.
- [48] M.S. Nadeem, T. Munawar, F. Mukhtar, A.W. Rabbani, N. ur Rehman, K. Mahmood, F. Iqbal, Facile synthesis of PANI and rGO supported Y/Pr co-doped ZnO: boosted solar light-driven photocatalysis, *Appl. Phys. A* 129 (2023) 1–14, <https://doi.org/10.1007/s00339-023-06701-2>.
- [49] Y. Chen, J. Qin, Y. Wang, Z. Li, Core/shell composites with polystyrene cores and meso-silica shells as abrasives for improved chemical mechanical polishing behavior, *J. Nanopart. Res.* 17 (2015), <https://doi.org/10.1007/s11051-015-3172-5>.
- [50] F. Mukhtar, T. Munawar, M.S. Nadeem, S.A. Khan, M. Koc, S. Batool, M. Hasan, F. Iqbal, Enhanced sunlight-absorption of Fe2O3 covered by PANI for the photodegradation of organic pollutants and antimicrobial inactivation, *Adv. Powder Technol.* 33 (2022), <https://doi.org/10.1016/j.apt.2022.103708>.
- [51] F. Mukhtar, T. Munawar, M.S. Nadeem, M.N. ur Rehman, M. Riaz, F. Iqbal, Dual S-scheme heterojunction ZnO-V2O5-WO3 nanocomposite with enhanced photocatalytic and antimicrobial activity, *Mater. Chem. Phys.* 263 (2021), <https://doi.org/10.1016/j.matchemphys.2021.124372>.
- [52] N. Xu, J. Ma, Q. Liu, W. Han, Z. Shan, Size effect of CeO₂ particle on nanoscale single-asperity sliding friction, *Tribology Lett.* 70 (2021), <https://doi.org/10.1007/s11249-021-01544-5>.
- [53] J. Ma, N. Xu, Y. Luo, Q. Liu, Y. Pu, Defect generation and morphology transformation mechanism of CeO₂ particles prepared by molten salt method, *Ceram. Int.* 49 (2023) 4929–4943, <https://doi.org/10.1016/j.ceramint.2022.10.007>.
- [54] Z. Wu, G. Li, Y. Jia, Q. Lv, S. Deng, Y. Jin, Investigation on morphology and chemistry of the Beilby layer on polished fused silica, *Ceram. Int.* (2023), <https://doi.org/10.1016/j.ceramint.2023.02.074>.
- [55] R. Peng, X. Sun, S. Li, L. Chen, M. Fu, J. Wu, D. Ye, Shape effect of Pt/CeO₂ catalysts on the catalytic oxidation of toluene, *Chem. Eng. J.* 306 (2016) 1234–1246, <https://doi.org/10.1016/j.cej.2016.08.056>.
- [56] J.P. Holgado, G. Munuera, J.P. Espinos, A.R. Gonzalez-Elipe, XPS study of oxidation processes of CeO_x defective layers, *Appl. Surf. Sci.* 158 (2000) 164–171, [https://doi.org/10.1016/s0169-4332\(99\)00597-8](https://doi.org/10.1016/s0169-4332(99)00597-8).
- [57] Y. Zhang, W. Zhu, L. Zhang, X. Gao, Y. Luo, J. Lu, Research progress on formation, characterization and mechanism of oxygen vacancies in cerium oxide, *J. Chin. Soc. Rare Earths* 40 (2021) 14–23, <https://doi.org/10.11785/s1000-4343.20220102>.
- [58] K. Mudiyanselage, H.Y. Kim, S.D. Senanayake, A.E. Baber, P. Liu, D. Stacchiola, Probing adsorption sites for CO on ceria, *Phys. Chem. Chem. Phys.* 15 (2013) 15856–15862, <https://doi.org/10.1039/c3cp52295d>.
- [59] S. Jiang, R. Zhang, H. Liu, Y. Rao, Y. Yu, S. Chen, Q. Yue, Y. Zhang, Y. Kang, Promoting formation of oxygen vacancies in two-dimensional cobalt-doped ceria nanosheets for efficient hydrogen evolution, *J. Am. Chem. Soc.* 142 (2020) 6461–6466, <https://doi.org/10.1021/jacs.9b13915>.
- [60] F. Jiang, S. Wang, B. Liu, J. Liu, L. Wang, Y. Xiao, Y. Xu, X. Liu, Insights into the Influence of CeO₂ Crystal Facet on CO₂ Hydrogenation to Methanol over Pd/CeO₂ Catalysts, *ACS Catal.* 10 (2020) 11493–11509, <https://doi.org/10.1021/acscatal.0c03324>.
- [61] J. Pan, S. Wang, A. Chen, Y. Chen, M. Wang, Y. Chen, Visible-light-active mesoporous ceria (CeO₂) nanospheres for improved photocatalytic performance, *J. Alloy. Compd.* 898 (2022), <https://doi.org/10.1016/j.jallcom.2021.162895>.
- [62] D. He, D. Chen, H. Hao, J. Yu, J. Liu, J. Lu, F. Liu, G. Wan, S. He, Y. Luo, Structural/surface characterization and catalytic evaluation of rare-earth (Y, Sm and La) doped ceria composite oxides for CH3SH catalytic decomposition, *Appl. Surf. Sci.* 390 (2016) 959–967, <https://doi.org/10.1016/j.apsusc.2016.08.129>.
- [63] S. Chahal, N. Rani, A. Kumar, P. Kumar, UV-irradiated photocatalytic performance of yttrium doped ceria for hazardous Rose Bengal dye, *Appl. Surf. Sci.* 493 (2019) 87–93, <https://doi.org/10.1016/j.apsusc.2019.06.284>.
- [64] L.M. Cook, Chemical process in glass polishing, *J. Non-Cryst. Solids* 120 (1990) 152–171, [https://doi.org/10.1016/0022-3093\(90\)90200-6](https://doi.org/10.1016/0022-3093(90)90200-6).
- [65] F. Mukhtar, T. Munawar, M.S. Nadeem, M.N. ur Rehman, K. Mahmood, S. Batool, M. Hasan, K. ur Rehman, F. Iqbal, Enhancement in carrier separation of ZnO-Ho2O3-Sm2O3 heterostructured nanocomposite with rGO and PANI supported direct dual Z-scheme for antimicrobial inactivation and sunlight driven photocatalysis, *Adv. Powder Technol.* 32 (2021) 3770–3787, <https://doi.org/10.1016/j.apt.2021.08.022>.
- [66] M. Wang, Z. Mu, T. Wang, Y. Chen, A. Chen, Double-layered core-shell heterostructures of mSiO₂/CdS@CeO₂ abrasive systems toward photochemical mechanical polishing (PCMP) applications, *Appl. Surf. Sci.* 614 (2023), <https://doi.org/10.1016/j.apsusc.2022.156274>.
- [67] A. Chen, S. Wang, J. Pan, T. Wang, Y. Chen, Development of Zr- and Gd-doped porous ceria (pCeO₂) abrasives for achieving high-quality and high-efficiency oxide chemical mechanical polishing, *Ceram. Int.* 48 (2022) 14039–14049, <https://doi.org/10.1016/j.ceramint.2022.01.289>.
- [68] A. Bayles, S. Tian, J. Zhou, L. Yuan, Y. Yuan, C.R. Jacobson, C. Farr, M. Zhang, D. F. Sweare, D. Solti, M. Lou, H.O. Everitt, P. Nordlander, N.J. Halas, Al@TiO₂ Core-Shell Nanoparticles for Plasmonic Photocatalysis, *ACS Nano* 16 (2022) 5839–5850, <https://doi.org/10.1021/acsnano.1c10995>.
- [69] C.M. Netzbando, K. Dunn, Investigation into the effect of CMP slurry chemicals on ceria abrasive oxidation state using XPS, *ECS J. Solid State Sci. Technol.* 8 (2019) P629–P633, <https://doi.org/10.1149/2.0311910jss>.
- [70] E. Kim, J. Hong, S. Hong, C. Kanade, H. Seok, H.-U. Kim, T. Kim, Improvement of oxide removal rate in chemical mechanical polishing by forming oxygen vacancy in

- ceria abrasives via ultraviolet irradiation, Mater. Chem. Phys. 273 (2021), <https://doi.org/10.1016/j.matchemphys.2021.124967>.
- [71] K.K. Myong, J. Byun, M.-j Choo, H. Kim, J.Y. Kim, T. Lim, J.J. Kim, Direct and quantitative study of ceria–SiO₂ interaction depending on Ce³⁺ concentration for chemical mechanical planarization (CMP) cleaning, Mater. Sci. Semicond. Process. 122 (2021), <https://doi.org/10.1016/j.mssp.2020.105500>.
- [72] C.M. Netzband, K. Dunn, Controlling the Cerium Oxidation State During Silicon Oxide CMP to Improve Material Removal Rate and Roughness, ECS J. Solid State Sci. Technol. 9 (2020), <https://doi.org/10.1149/2162-8777/ab8393>.